Properties of GaN and related compounds studied by means of Raman scattering

2002 J. Phys.: Condens. Matter 14 R967

(http://iopscience.iop.org/0953-8984/14/38/201)

INSTITUTE OF PHYSICS PUBLISHING JOURNAL OF PHYSICS: CONDENSED MATTER

J. Phys.: Condens. Matter **14** (2002) R967–R993 PII: S0953-8984(02)24668-8

TOPICAL REVIEW

Properties of GaN and related compounds studied by means of Raman scattering

Hiroshi Harima

Department of Electronics and Information Science, Kyoto Institute of Technology, Matsugasaki, Sakyo-ku, Kyoto 606-8585, Japan

E-mail: harima@dj.kit.ac.jp

Received 10 December 2001, in final form 13 August 2002
Published 12 September 2002
Online at stacks.iop.org/JPhysCM/14/R967

Abstract

In the last decade, we have seen very rapid and significant developments in Raman scattering experiments on GaN and related nitride compounds: the Γ-point phonon frequencies have been identified for both cubic and hexagonal structures of binary compounds of GaN, AlN, and InN. The phonon spectra of their ternary alloys, InGaN and AlGaN, were also intensively studied. On the basis of these studies, characterizations of strain, compositional fluctuation, defects, impurities, etc, are now being intensively conducted. Besides such pure lattice properties, coupled modes between a lattice vibration (LO phonon) and a collective excitation of free carriers (plasmon) in GaN have been thoroughly studied, and the results are now widely applied to characterize carrier-transport properties. Low-dimensional structures of nitrides such as quantum dots and superlattices will soon enter the most active field of Raman scattering characterization. This article briefly reviews the present status of Raman scattering experiments on GaN and related nitride compounds and presents some future prospects.

(Some figures in this article are in colour only in the electronic version)

Contents

1. Introduction 968
2. Lattice properties 969
   2.1. AlN, GaN, and InN 969
   2.2. AlGaN and InGaN 974
   2.3. The stress effect 977
   2.4. Defect and impurity modes 978
   2.5. Phonon-related topics—temperature effects, superlattices, dilute magnetic semiconductors 982

3. Electronic properties 983
3.1. LO phonon–plasmon coupled modes 983
3.2. Inter-valence-band transitions 986
4. Other topics 986
4.1. Resonant Raman scattering—quantum wells, quantum dots 986
4.2. Micro-Raman imaging 987
5. Concluding remarks 989
References 989

1. Introduction

This article reviews recent Raman scattering experiments on nitride semiconductors. Before going into the details, let us introduce some basic characteristics. Table 1 shows selected properties of binary nitride compounds that are treated in this article [1–3]. The three species, AlN, GaN, and InN, crystallize in both hexagonal (wurtzite) and cubic (zinc-blende) structures. Since the wurtzite materials are more stable than other and direct-transition-type semiconductors, they have garnered much attention as attractive candidates for use as light emitters or detectors. They can cover continuously, by appropriate alloying, from 1.9 eV (the bandgap of hexagonal InN) to 6.2 eV (the bandgap of hexagonal AlN). (It should be noted here, however, that a much smaller bandgap of hexagonal InN, 0.7–0.9 eV, has been reported very recently from optical experiments using high-quality epitaxial films [4, 5], which means that the value should be re-examined urgently.) In the mid-1990s, light-emitting diodes (LED) for the blue and green regions of the spectrum were commercialized. Then, a few years later, blue lasers emitting at 405 nm were commercialized. Besides those in optical devices, applications in high-power and high-frequency electronic devices have also garnered much attention. This is because the materials show relatively high electron saturation velocity and high breakdown field: for example, GaN shows an electron saturation velocity 2 to 3 times higher than that of Si ($\sim 1 \times 10^7$ cm s^{-1}), and a breakdown field one order or more greater than that in Si ($\sim 3 \times 10^5$ V s^{-1}) [6]. Quite recently, various prototype electronic devices based on nitride semiconductors such as the HEMT (high-electron-mobility transistor) have been fabricated. For detailed information on the growth, processing, characterization, and device developments, see the respective review articles [1–3, 7–10].

Raman scattering is a standard optical characterization technique for studying various aspects of solids such as lattice properties, electronic properties, and magnetic properties. Raman scattering has many advantages when compared with other spectroscopic techniques: it is in principle non-destructive, contactless, and requires no special sample preparation technique such as thinning or polishing. Furthermore, when a standard Raman microscope is used with a visible laser for excitation, we can obtain lateral resolution of ~ 1 μm or less, which is determined by the beam waist of the probe laser at the sample surface. Raman scattering occurs essentially as a result of modulation of the electronic polarizability induced by various elementary excitations in solids such as phonons and plasmons. In the case of Raman scattering by phonons, the scattering efficiency is higher in covalent crystals than in ionic crystals, because the valence electrons are less localized and larger fluctuation of the polarizability can be induced by lattice vibration. From this viewpoint, nitride semiconductors are suitable for Raman scattering studies, since the chemical bonding is a mixture of covalent and ionic bonding. Furthermore, nitride semiconductors are generally robust and stand up well to laser irradiation, which is another advantage of Raman scattering studies.

Table 1. Basic properties of the three nitrides [1–3].

	AlN	GaN	InN	Unit
Hexagonal (wurtzite)				
Density	3.23	6.15	6.81	g cm^{-3}
Bandgap (E_g)	6.2	3.39	1.89c	eV (at 300 K)
Temperature dependence (dE_g/dT)	—	−6	−1.8	10^{-4} eV K^{-1}
Pressure dependence (dE_g/dP)	—	4.2	—	10^{-3} eV kbar^{-1}
Lattice constant[a]	$a = 3.11$	$a = 3.189$	$a = 3.54$	10^{-8} cm
	$c = 4.98$	$c = 5.185$	$c = 5.70$	10^{-8} cm
Thermal expansion coefficient[a]	$\Delta a/a = 4.2$	$\Delta a/a = 5.59$	$\Delta a/a \sim 4$	10^{-6} K^{-1}
	$\Delta c/c = 5.3$	$\Delta c/c = 3.17$	$\Delta c/c \sim 3$	10^{-6} K^{-1}
Deformation potential	9.5	8.3	7.1	eV
Thermal conductivity	2	1.3	0.8	W cm^{-1} K^{-1}
Refractive index	2.15 (at 3 eV)	2.33 (at 1 eV)	2.9–3.05	
		2.67 (at 3.38 eV)		
Dielectric constant	$\varepsilon_\infty = 4.77$	$\varepsilon_\infty = 5.35$	$\varepsilon_\infty = 8.4$	
	$\varepsilon_0 = 8.5$	$\varepsilon_0 = 8.9$–9.5	$\varepsilon_0 = 15.3$	
Electron effective mass	0.48	0.2	0.11	m_0
Electron saturation velocity	1.4	2.5	2.5	10^7 cm s^{-1}
Breakdown field	—	>5	—	10^6 V s^{-1}
Cubic (zinc-blende)				
Bandgap (E_g)	5.11[b]	3.2–3.3	2.2	eV (at 300 K)
Lattice constant	$a = 4.38$	$a = 4.52$	$a = 4.98$	10^{-8} cm
Refractive index	—	2.9 (3 eV)	—	

[a] For comparison, sapphire has lattice constants of $a = 4.758$ and $c = 12.9991 \times 10^{-8}$ cm, thermal expansion coefficients $\Delta a/a = 7.5$ K^{-1} and $\Delta c/c = 8.5 \times 10^{-6}$ K^{-1}, and thermal conductivity of 0.5 W cm^{-1} K^{-1}.
[b] Theoretical value (indirect bandgap).
[c] Very recently, a much smaller bandgap (0.7–0.9 eV) has been reported [4, 5].

The following consists of three parts: sections 2 and 3 describe Raman scattering studies related to lattice properties and electronic properties, respectively, and section 4 describes some important topics from the viewpoint of experimental techniques.

2. Lattice properties

2.1. AlN, GaN, and InN

This section starts with a brief introduction to the phonon dispersion of nitride semiconductors. As described in the previous section, the group-III nitrides crystallize in hexagonal (wurtzite; space group C_{6v}^4) or cubic structure (zinc-blende; T_d^2). Here, let us take GaN as an example: in the hexagonal structure, the primitive cell contains two Ga–N atom pairs, while it contains only one atom pair in the cubic structure. In both cases, a Ga atom is tetrahedrally surrounded by four N atoms, and vice versa. The hexagonal and cubic structures differ only in the stacking sequence of the Ga–N bilayers along the cubic [111] direction, which coincides with the hexagonal [0001] direction. That is, the stacking order is ABCABC... in the cubic structure, while it is ABAB... in the hexagonal structure. Here A, B, and C denote the allowed sites of the Ga–N pair in the close-packed layer of spheres. The unit-cell length of the cubic structure along [111] is given by the width of one unit bilayer, while that of the hexagonal structure along [0001] is double that. Therefore, as shown schematically in figure 1, the phonon dispersion of the hexagonal structure along [0001] ($\Gamma \rightarrow$ A in the Brillouin zone) is approximated by

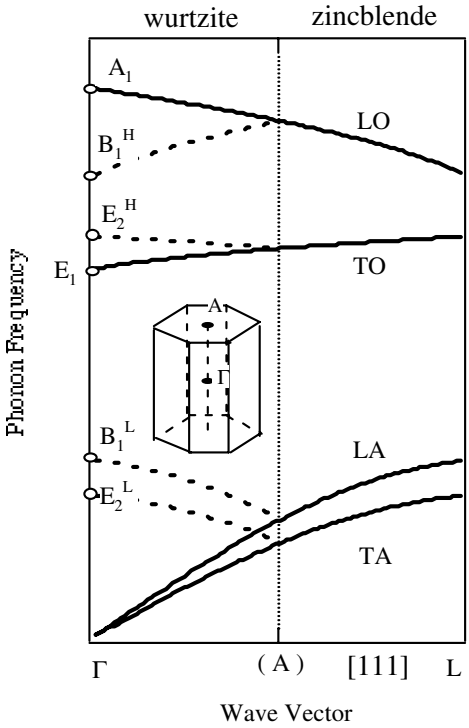

Figure 1. Schematic representation of the phonon dispersion. Phonon branches along [111] in the zinc-blende structure are folded to approximate those of wurtzite structure along [0001].

folding the phonon dispersion of the cubic structure along [111] ($\Gamma \rightarrow$ L). By this folding, the TO phonon mode at the L point of the Brillouin zone in the cubic structure reduces to the E_2 mode at the Γ point of the Brillouin zone in the hexagonal structure. This mode is denoted in figure 1 as E_2^H, where the superscript H means the higher-frequency branch of the E_2 phonon mode. There is another E_2 mode at lower frequency labelled as E_2^L, which derives from zone folding of the transverse acoustic (TA) mode in the cubic structure. In the hexagonal structure, there is anisotropy in the macroscopic electric field induced by polar phonons. Thus, both the TO and LO modes split into the axial (or A_1) and planar (or E_1)-type modes where atomic displacement occurs along the *c*-axis or perpendicular to the *c*-axis, respectively. This splitting is not shown in figure 1.

The first-order phonon Raman scattering is caused by phonons with wavevector $\boldsymbol{k} \sim 0$ (Γ point) because of a momentum conservation rule in the light scattering process. In the hexagonal structure, group theory predicts eight sets of phonon normal modes at the Γ point, $2A_1 + 2E_1 + 2B_1 + 2E_2$. Among them, one set of A_1 and E_1 modes are acoustic, while the remaining six modes, $A_1 + E_1 + 2B_1 + 2E_2$, are optical. As shown in figure 1, one A_1 and one B_1 mode (B_1^H) derive from a singly degenerate LO phonon branch of the cubic system by zone folding, while one E_1 and one E_2 mode (E_2^H) derive from a doubly degenerate TO mode in the cubic system. The atomic displacement scheme of these optical modes is shown in figure 2. The A_1 and B_1 modes give atomic displacements along the *c*-axis, while the others, E_1 and E_2, give atomic displacements perpendicular to the *c*-axis, Here, the A_1 and E_1 modes are both Raman and infrared (IR) active, while the two E_2 modes are only Raman active, and the two B_1 modes are neither Raman nor IR active (silent modes) [11].

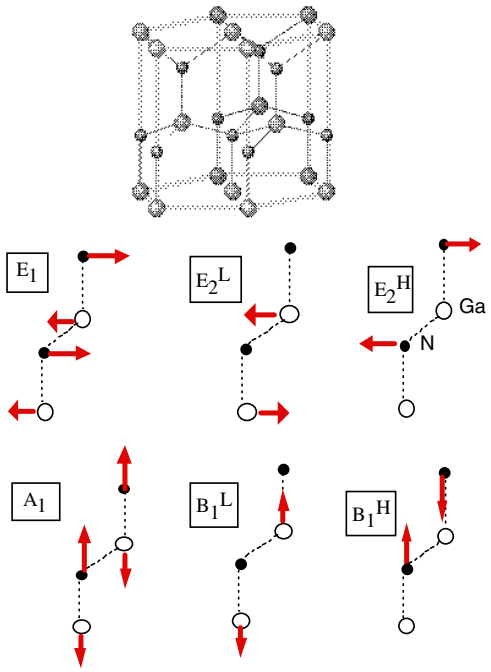

Figure 2. Optical phonon modes in the wurtzite structure. There are two types of the E_2- and B_1-type modes that are distinguished by superscripts L and H.

The Raman scattering efficiency S with polarization detection is given by

$$S \propto |\boldsymbol{e}_L \mathbf{R} \boldsymbol{e}_S|^2 \tag{1}$$

where $\boldsymbol{e}_L$ and $\boldsymbol{e}_S$ denote polarization for the incident and scattered light, respectively, and $\mathbf{R}$ is the Raman tensor of the scattering process. In the case of wurtzite structure, the Raman tensor only has diagonal components for the A_1 phonon mode, while there are only off-diagonal components for the E_1 mode and both diagonal and off-diagonal components for the E_2 mode [12]. This means that the A_1 mode can be observed when the incident and scattered light have parallel polarization, while the E_1 mode is observed only in crossed polarization geometry. Table 2 summarizes the scattering geometries for observing the Raman-active modes in the wurtzite structure. Here, conventional notation is used to describe the scattering geometry: outside the bracket, the symbols show from left to right the direction of incident and scattered light, respectively, and inside the bracket, they give from left to right the polarization direction of the incident and scattered light, respectively. The A_1(LO) phonon mode has atomic displacement parallel to the c-axis, and propagates along the c-axis. Therefore, taking the z-direction along the c-axis and x- and y-directions perpendicular to the c-axis, the A_1(LO) mode can be observed from backscattering from the c-plane of wurtzite samples by taking the $z(x, x)\bar{z}$ scattering configuration. On the other hand, Raman selection rules for the zinc-blende-type crystals are relatively simple: if backscattering geometry is employed with no polarization detection, only the LO phonon is observed from the (100) plane, while only the TO phonon is observed from the (110) plane. The TO and LO phonons are simultaneously observed from backscattering from the (111) plane [11].

Figure 3 shows typical phonon spectra of a hexagonal GaN layer grown on a sapphire (1000) substrate [13]. The upper result was obtained by back scattering from the c-plane with

Table 2. Raman configurations of allowed modes in hexagonal nitrides.

Configuration	Mode
$x(y, y)\bar{x}$	A_1(TO), E_2
$x(z, z)\bar{x}$	A_1(TO)
$x(z, y)\bar{x}$	E_1(TO)
$x(y, z)y$	E_1(TO), E_1(LO)
$x(y, y)z$	E_2
$z(y, x)\bar{z}$	E_2
$z(y, y)\bar{z}$	A_1(LO), E_2

no polarization detection, where two E_2 phonon peaks (E_2^L, E_2^H) and one LO phonon peak, A_1(LO), are observed. A substrate signal is also weakly observed at 418 cm $^{-1}$. The higher-frequency E_2 mode (E_2^H) is the strongest, and is common to hexagonal GaN, InN, and AlN. The lower result was obtained from backscattering from the cross-section of the layer using parallel (upper) and crossed (lower) polarization detection, where the A_1(TO) and E_1(TO) modes give the dominant features, respectively.

The first-order phonon Raman spectra and Γ-point phonon frequencies have been intensively studied for hexagonal GaN [14–22] and AlN [14, 23–28]. On the other hand, experiments on cubic GaN [22, 29], cubic AlN [30], and cubic and hexagonal InN [31–33] are scarce because of the difficulty of sample preparation. Typical phonon frequencies observed by means of Raman scattering are listed in table 3 [14, 19, 29–32]. Since these values were mostly derived for hetero-epitaxial films, the frequencies are somewhat influenced by residual stresses. It is very difficult, however, to precisely estimate this effect because it depends on the growth conditions. Table 3 lists the substrate species and the film thickness for each sample for consideration of this. Roughly speaking, residual stress can be neglected for films thicker than ∼10 μm: for example, hexagonal GaN films with thickness 50–70 μm [14] give phonon frequencies very close to those of bulk samples [19], as seen from the comparison in table 3. On the other hand, for relatively thin samples with thickness less than ∼1 μm, such as the cubic samples in table 3, the strain effect cannot be neglected. It is estimated that the phonon frequencies may be affected within ∼1 cm^{-1} by the residual stress, if thermal expansion coefficients equal to those of the hexagonal system are assumed for comparison with those of the substrates [1].

In the bottom spectrum of figure 3 for geometry $x(z, y)\bar{x}$, the A_1(TO) and E_2^H modes are weakly observed although they are forbidden. Similarly, the E_1(LO) mode—quasi-E_1(LO)—is weakly observed in the forbidden geometry $x(z, z)\bar{x}$. This effect, i.e., relaxation of the Raman selection rule, may be attributed to a large solid angle of the objective lens of the Raman microscope (the so-called leakage effect). The reason is as follows: GaN belongs to a system where long-range electrostatic force predominates over the crystalline anisotropy, as easily understood from the fact that the TO–LO splitting (180–200 cm^{-1}) is much larger than the A_1–E_1 splitting (7–30 cm^{-1}) [12]. In such a system, mixing of A_1 and E_1 modes may easily occur when the incident or the scattered radiation is not strictly parallel or perpendicular to the optical axes [21, 22, 34, 35]. Since the wurtzite nitrides are uniaxial crystals, purely transverse or longitudinal phonons with A_1 or E_1 symmetry can be observed only when the phonon propagation direction is strictly parallel or perpendicular to the crystal axis. For an intermediate propagation direction, therefore, mixing of A_1 and E_1 modes occurs, yielding quasi-TO and quasi-LO modes. They have some intermediate frequency values as follows [12, 34, 36, 37]:

$$\omega_Q^2(\mathrm{TO}) = \omega^2(\mathrm{E_1[TO]})\cos^2\theta + \omega^2(\mathrm{A_1[TO]})\sin^2\theta \tag{2}$$

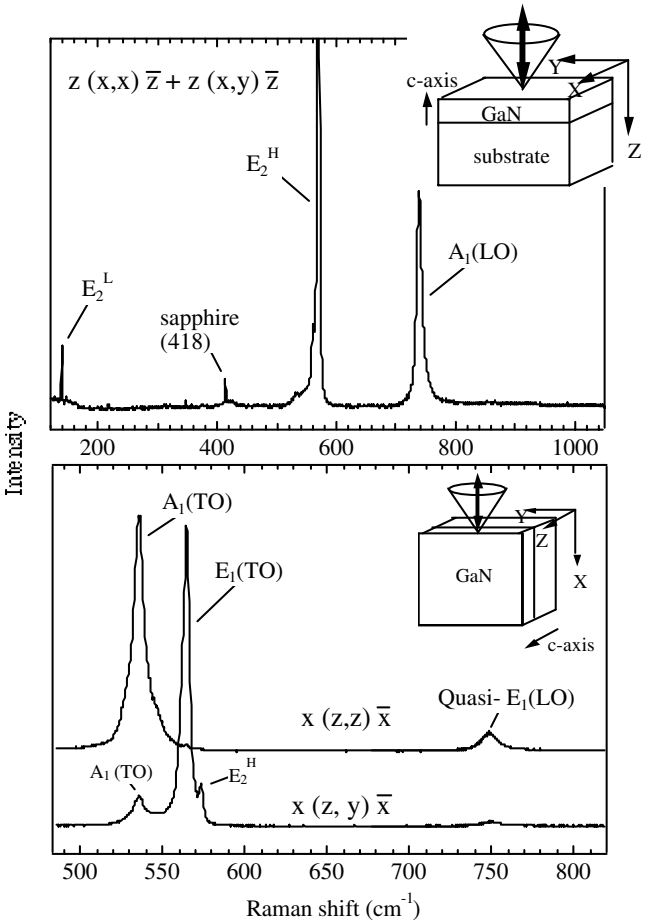

Figure 3. Typical Raman spectra of hexagonal GaN observed at different scattering geometries [13]. The inset shows schematically the directions of the incident and scattered light. The substrate (sapphire) signal appears weakly at 418 cm^{-1}.

$$\omega_Q^2(\mathrm{LO}) = \omega^2(\mathrm{A_1[LO]})\cos^2\theta + \omega^2(\mathrm{E_1[LO]})\sin^2\theta. \tag{3}$$

Here, θ is the angle between the c-axis and the phonon propagation direction. The quasi-E_1(LO) mode (figure 3) has almost pure E_1(LO)-mode character, since the frequency agrees well with that observed in the allowed geometry, $x(y, z)y$.

So far, only the first-order Raman scattering has been considered. With the advent of high-quality crystals, it has become possible to observe precise second-order phonon spectra of hexagonal GaN [37, 38] and AlN [14]. For second-order Raman scattering, the momentum conservation rule demands that the sum of the wavevectors of the two phonons participating in the Raman scattering process is zero: $\boldsymbol{k}_1+\boldsymbol{k}_2 \sim 0$. Thus, the phonon modes that contribute to the Raman scattering are not limited to those at the Γ point, but extend to the whole Brillouin zone. In this sense, second-order phonon Raman spectra reflect the phonon density of states, and can be regarded as a critical test of the calculated phonon dispersion curve [14, 31, 37, 39, 40]. A group theory analysis of the GaN spectrum revealed that acoustic overtones appeared at 300–420 cm^{-1}, acoustic–optical combinations at 850–1000 cm^{-1}, and optical overtones and combination modes at 1150–1500 cm^{-1} [37]. Similar results were obtained for AlN [14].

Table 3. Typical phonon frequencies (cm^{-1}) observed at 300 K for hetero-epitaxial nitride films. The values in brackets derive from bulk samples [19].

	AlN	GaN	InN
Hexagonal (wurtzite)			
E_2^L	248.6	144 (144)	87
A_1(TO)	611	531.8 (531)	447
E_1(TO)	670.8	558.8 (560)	476
E_2^H	657.4	567.6 (568)	488
A_1(LO)	890	734	586
E_1(LO)	912	741	593
Substrate	Sapphire	Sapphire	Sapphire
Thickness (μm)	50–70	50–70	0.1–0.7
Reference	[14]	[14, 19]	[31]
Cubic (zinc-blende)			
TO	655	555	472
LO	902	742	586
Substrate	3C-SiC	GaAs	GaAs
Thickness (μm)	0.1–0.4	1	1
Reference	[30]	[29]	[32]

2.2. AlGaN and InGaN

As described in the introduction (section 1), growing high-quality ternary alloys of $Al_xGa_{1-x}N$ and $In_xGa_{1-x}N$ is a key technology for fabricating light-emitting devices operating in the visible-to-UV region. For example, Nakamura fabricated diode lasers with the emission wavelength ∼405 nm using an $In_{0.2}Ga_{0.8}N/In_{0.05}Ga_{0.95}N$ multiple-quantum-well (QW) structure for the active region, and $Al_{0.12}Ga_{0.88}N$ layers for the cladding layers [41]. Raman spectroscopy can clarify various aspects of the lattice and electronic properties in such alloy systems; e.g., atomic composition as well as its homogeneity, residual stress, electronic band structure, carrier concentration. The observation of phonon spectra at different atomic compositions, which is described in this section, is the first step for such characterizations.

Let us first look at the case of $Al_xGa_{1-x}N$. In the ideal case of an alloy, N atoms occupy all the anion sites, while Al and Ga atoms share the cation sites in a random manner with a probability ratio $x:(1-x)$. Since phonon Raman spectra are in general sensitive to disorder in atomic arrangements, such randomness yields broadening of the phonon spectral peaks. Unexpected peaks may also appear because the Raman selection rule is relaxed by this randomness. Furthermore, the phonon frequency may shift with the atomic composition, since the average reduced mass of the anion and cation pair changes, and there are often two types of characteristic behaviour: one is the so-called one-mode-type behaviour, in which the $\boldsymbol{k} \sim 0$ phonon frequency varies continuously from the mode frequency of one end-member to that of the other, and appears with approximately constant strength; the other is the two-mode-type behaviour, in which for an intermediate alloy composition two sets of phonon frequencies appear at frequencies close to those of the end-members, the strength of each mode being approximately proportional to the mole fraction of each component. Let us examine such an example.

Figures 4(a) and (b) show the variation of the phonon spectra in cubic $Al_xGa_{1-x}N$ from $x = 0$ (GaN; bottom) to $x = 1$ (AlN; top) for the TO and LO phonon regions, respectively [30]. Here, epitaxial films with thickness 0.1–0.4 μm grown on 3C-SiC/Si substrate were observed. The arrows denote the TO and LO phonon modes of the $Al_xGa_{1-x}N$ alloys, while the other

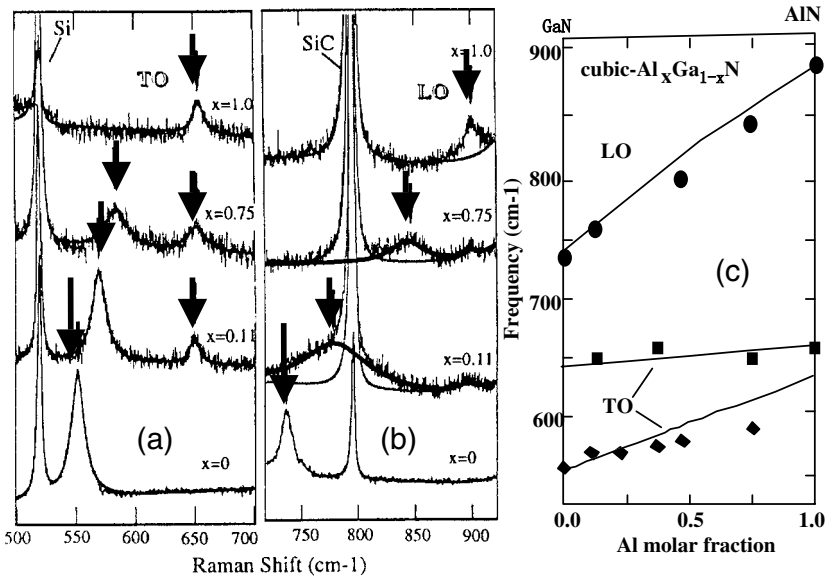

Figure 4. Raman spectra of cubic $Al_xGa_{1-x}N$ layers grown on 3C-SiC/Si [30]. Here, (a) and (b) correspond to the TO- and LO phonon regions, respectively. The phonon frequency is plotted in (c) along with a calculation made using the REI model (solid curves).

phonon signals derive from the substrate (Si; 520 cm^{-1}; 3C-SiC; 796 cm^{-1}). The observed phonon frequencies are plotted in figure 4(c) against x by filled symbols. It is seen that the LO phonon frequency varies smoothly from GaN to AlN on one curve (one-mode behaviour), while the TO mode varies on two isolated paths starting from $x = 0$ (the GaN-like mode) and from $x = 1$ (the AlN-like mode); that is, the TO mode shows two-mode behaviour. It is also found that the phonon peaks are heavily broadened in the intermediate range of x; this derives from the compositional fluctuation. The solid curves in figure 4(c) represent a theoretical calculation of the alloy mode frequencies based on a random-element isodisplacement (REI) model [42, 43]. The theory correctly predicts the different mode behaviours of the TO and LO modes, and attributes the one-mode behaviour of the LO phonon to its sensitivity to the surrounding electric field and to there being strong ionicity in the cation–nitrogen bond.

Hexagonal $Al_xGa_{1-x}N$ gives much more complicated features than the cubic system, as expected from the rich phonon structure of hexagonal binary compounds. Some groups reported phonon data based on Raman scattering [44, 45] and IR absorption [46]. A comprehensive study based on Raman scattering was recently reported by Davydov *et al* [47], part of which is illustrated in figure 5. The authors used a large set of samples including 2–4 μm thick films with $0 < x < 0.5$ grown on sapphire, and 1–4 μm thick films with $0.5 < x < 1$ grown on Si(111). Both the A_1(LO) and E_1(LO) modes showed one-mode behaviour, while the others, A_1(TO), E_1(TO), E_2^H, and E_2^L, showed two-mode behaviour. If we recall that the phonon dispersion of wurtzite nitride is closely connected to that of zinc-blende nitride, by zone folding (see figure 1), these results are consistent; LO modes tend to show one-mode behaviour, while others show two-mode behaviour. The authors proposed quadratic equations to fit the observed frequency as follows (in cm^{-1}): A_1(LO): $734 + 153x + 75x(1-x)$; E_1(LO): $742 + 170x + 65x(1-x)$; A_1(GaN-like TO): $531.8 + 64.5x - 1.9x(1-x)$; and E_2 (low, GaN-like): $142.8 + 43.5x - 14.5x(1-x)$ [47]. The small bowing parameters for the latter two

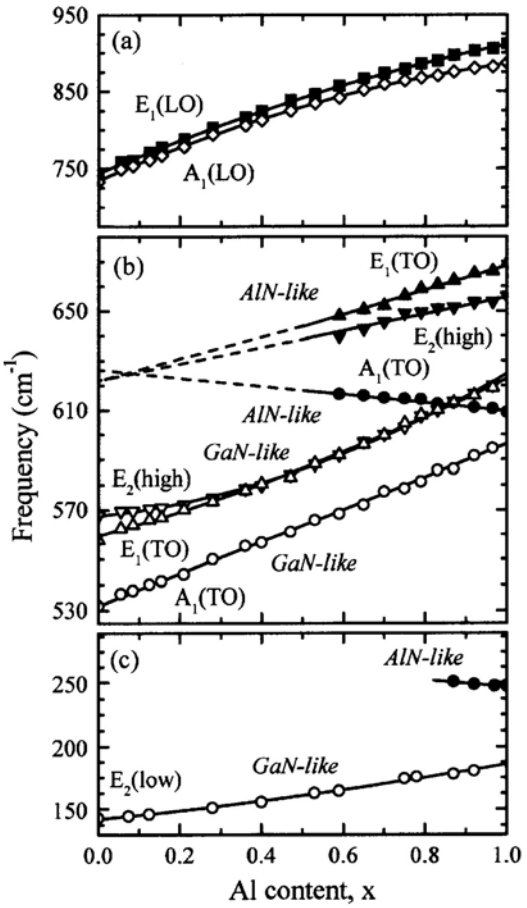

Figure 5. The compositional dependence of phonon frequencies in hexagonal $Al_xGa_{1-x}N$ [47].

(1.9 and 14.5) indicate almost straight variations and, thus, these equations are very convenient for estimating x from Raman spectra. It should be noted here that strain effects which also depend on x should be included in a rigorous discussion of the relation between the phonon frequency and the atomic composition. This remains, however, for the future. Davydov *et al* also analysed the broadening of phonon peaks with x, considering the process of elastic scattering of phonons by the compositional fluctuation.

In the case of $In_xGa_{1-x}N$, on the other hand, phonon spectra have been reported only for a limited range of atomic composition. This is mainly because a phase-separation problem has long prevented the growth of high-quality In-rich crystals [9]. (The large difference in interatomic spacing between GaN and InN gives rise to a solid phase miscibility gap: spinodal decomposition occurs typically at $x \gtrsim 0.3$ in $In_xGa_{1-x}N$ films grown at 700–800 °C with thickness $\sim$0.5 μm, though this problem can be suppressed in much thinner films.) Successful growth of hexagonal epitaxial films with $0.5 < x < 1$ was recently reported along with photoluminescence (PL) and absorption data [48, 49]. However, phonon data are still very limited; they are available just for hexagonal $In_xGa_{1-x}N$ with $x = 0$–0.33 [50] and 0–0.07 [51], and cubic $In_xGa_{1-x}N$ with $x = 0$–0.31 [52]. According to the results, both the TO and LO modes in hexagonal and cubic systems show one-mode behaviour. This is clearly different

from the case for $Al_xGa_{1-x}N$, where one-mode behaviour was observed only for the LO mode [30, 46]. This indicates that the TO phonons show either one- or two-mode behaviour depending on the cation size [43]: the reduced mass of the In–N pair (12.5 amu) comes closer to that of GaN (11.7) than that of AlN (9.2). Consequently, the In–N atomic pair follows the frequency of the Ga–N pair vibration more easily than the Al–N pair does. Therefore, TO phonons in $Al_xGa_{1-x}N$ tend to show independent modes in the intermediate composition range. The difference in phonon kinetics between the cubic and hexagonal system is not essential. However, such a simple picture does not hold for the LO mode, where a long-range electrostatic force deriving from the strong ionicity of the cation–nitrogen bond dominates the difference in reduced mass. Thus, one-mode-type behaviour is preferred for the LO phonon mode in both $Al_xGa_{1-x}N$ and $In_xGa_{1-x}N$ in either the cubic or hexagonal structure form.

2.3. The stress effect

As is well known, residual strain in layered structure is an important issue in fabricating opto-electronic devices. As a typical example, strain in a laser diode structure may change the electronic band structure in the optically active region and affect the laser gain [53]. There are several causes of the lattice strain: first, lattice mismatch and difference in thermal expansion coefficient between hetero-epitaxial layers or between a deposited layer and its substrate may cause in-plane uniaxial or biaxial strain; second, lattice structure may be distorted in the neighbourhood of native defects or by incorporated impurities. These point defects will induce a three-dimensional strain such as hydrostatic stress if the defects are uniformly distributed. Generally, hydrostatic strain and uniaxial or biaxial strain may coexist in hetero-epitaxial layers. For more general aspects of the strain effect in nitride layers, see the appropriate review articles [54–56].

Let us introduce some Raman studies on hydrostatic stress in hexagonal AlN [23, 24, 28, 55] and GaN [19, 52] conducted by using diamond anvil cell for pressure loading. The results are summarized in table 4, where the linear stress-shift coefficients K and the mode Grüneisen parameters γ are listed [54, 57]. Here, K is defined by $\omega = \omega_0 K p$, where p is the applied hydrostatic pressure in GPa, and ω (ω_0) is the phonon frequency with (without) pressure. The mode Grüneisen parameter is a ratio between the frequency-shift rate $d\omega/\omega_0$ and the volume compression dV/V, which can be rewritten using the bulk modulus B_0 as

$$\gamma = (d\omega/\omega_0)/(dV/V) = (B_0/\omega_0)(d\omega/dp). \tag{4}$$

Perlin and co-workers obtained γ by using experimental data for K and putting $B_0 = 210$ and 207.9 GPa for GaN and AlN, respectively [28, 54]. A peculiar feature seen in table 4 is that the E_2^L phonon mode of GaN takes negative values of K and γ; recalling that the E_2^L phonon mode at the Γ point of the Brillouin zone of the hexagonal structure is approximated by zone folding of the zone-boundary (L-point) TA phonon in the cubic structure (see figure 1), Perlin and co-workers connected this negative pressure dependence, or soft-mode behaviour, to a softening of the TA phonon of cubic GaN [19, 28, 54]. In fact, a phase transition occurs from wurtzite to rock-salt structure at 47 and 16.6 GPa in GaN and AlN, respectively [19, 58].

Next, biaxial strain in nitride layers is considered. If wurtzite layers are hetero-epitaxially grown on some hexagonal (0001) or cubic (111) substrates, the layers will have uniform biaxial strain in the c-plane with strain tensor components $\varepsilon_{xy} = \varepsilon_{yz} = \varepsilon_{zx} = 0$, $\varepsilon_{xx} = \varepsilon_{yy} \neq 0$, and $\varepsilon_{ZZ} \neq 0$. That is, the layers are uniformly compressed or expanded in the c-plane, and in the reverse manner along the c-axis. In this case, the wurtzite (C_{6v}) symmetry is maintained. Therefore, there is no change in the list of phonon modes, and only a phonon frequency shift is

Table 4. The hydrostatic pressure shift of the phonon modes. K (the linear stress-shift coefficient) and γ (the mode Grüneisen parameter) are shown. See the text for their definitions. (Asterisks mark quasi-LO modes).

Wurtzite	E_2^L	A_1(TO)	E_1(TO)	E_2^H	A_1(LO)	E_1(LO)	Unit	Reference
GaN								[54]
K	−0.32	3.8	3.3	3.6	3.8	—	cm^{-1} GPa^{-1}	
γ	−0.46	1.5	1.24	1.33	1.09	—		
AlN								[57]
K	—	4.08	5.07	5.39	4.00	5.51*	cm^{-1} GPa^{-1}	
γ	—	1.39	1.57	1.71	0.93	1.26*		

expected. As an example, let us examine hexagonal GaN layers grown on sapphire (0001) and 6H-SiC (0001). Sapphire has a larger thermal expansion coefficient ($a_\perp = 7.5 \times 10^{-6}$ K^{-1}) than GaN ($a_\perp = 5.59 \times 10^{-6}$ K^{-1}) [59]. Thus, considering that only the difference in thermal expansion coefficient induces the stress, compressive strain will be generated in the GaN c-plane in the process of cooling from the growth temperature to room temperature. In contrast, if 6H-SiC is used as the substrate, the result is reversed, since 6H-SiC has a smaller thermal expansion coefficient ($a_\perp = 4.2 \times 10^{-6}$ K^{-1}) than GaN [60].

Biaxial strain in the c-plane of the hexagonal GaN layer is most easily probed by observing the E_2^H phonon mode by means of Raman scattering [34, 61–63]; this is because the frequency is sensitive to biaxial strain in the c-plane as expected from the atomic displacement scheme (figure 2) and, furthermore, this mode conveniently gives the strongest signal in the spectra (figure 3). Demangeot *et al* [63] observed the stress shift for the A_1(LO) mode and the E_2^H mode in hexagonal GaN as plotted in figure 6. The authors evaluated the stress-shift rate as 0.8 cm^{-1} GPa^{-1} for the A_1(LO) mode and 2.9 cm^{-1} GPa^{-1} for the E_2^H mode. Some other groups also reported stress-shift rates for the E_2^H mode: 6.2 [62], 4.2 [61], and 2.7 cm^{-1} GPa^{-1} [34]. These experimental results show scatter due to the difference in evaluation method of biaxial stress; i.e., PL or reflection for the excitonic transition [61, 63], x-ray diffraction to determine the lattice constant [34], surface profilometry to get the wafer curvature [62]. They were analysed with relevant elastic constants assumed. A theoretical value from first-principles calculation, 2.4 cm^{-1} GPa^{-1} [64], agrees well with the relatively small experimental values, 2.7 [34] and 2.9 cm^{-1} GPa^{-1} [63]. Davydov *et al* [34] reported biaxial stress-shift rates for the E_2^L, A_1(TO), and E_1(TO) modes of GaN: −0.5, 2.8, and 1.4 cm^{-1} GPa^{-1}, respectively.

2.4. Defect and impurity modes

So far, only phonon signals related to the host lattice have been described. In fact, however, we can often observe foreign signals induced by impurities. If impurity atoms replace host-lattice atoms heavier than the impurities, atomic oscillation may be induced in a limited range around the impurities, which is the so-called local vibrational mode (LVM). Its frequency appears in the energy gap between the acoustic and optical branches of phonons, or above the optical branch. As the impurity is lighter, the LVM frequency becomes higher and the vibration is more localized [65]. Another typical foreign signal derives from defects; i.e., the defect mode. Point defects such as vacancies can cause a defect mode with a sharp peak like the LVM. On the other hand, heavily disordered systems such as ion-implanted or low-temperature-grown crystals can exhibit a different type of defect mode called the disorder-activated Raman scattering (DARS) mode. DARS occurs as a result of phonon confinement to small (typically less than 100 nm) defect-free regions. This confinement relaxes the Raman selection rules,

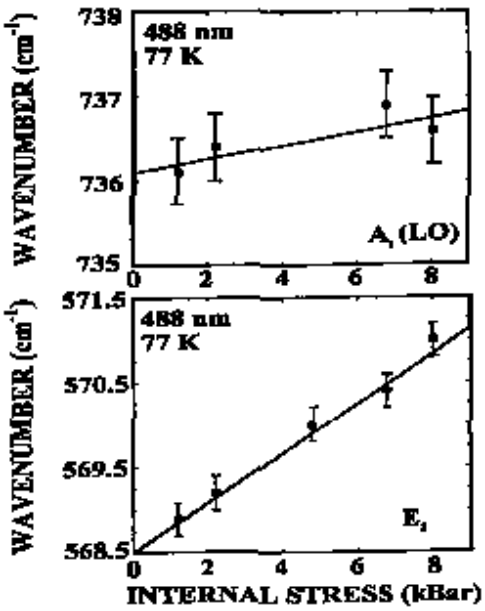

Figure 6. Stress shifts of the $A_1(LO)$ and E_2^H phonon modes in hexagonal GaN grown on sapphire substrate [63]. Lines denote the best linear fits to the data.

allowing phonons with non-zero wavevectors to contribute to first-order Raman scattering. The DARS reflects, therefore, the phonon density of states of the host lattice, and usually appears with broad spectral features. In the following, a LVM in Mg-doped GaN is first introduced to demonstrate that a LVM can yield valuable information on the microscopic processes in solids. Defect modes in ion-implanted GaN are then briefly described.

It is well known that low-energy electron beam irradiation [66] or thermal annealing in a N_2 atmosphere [67] is necessary to obtain p-type conductivity in Mg-doped GaN films grown by MOCVD (metal–organic chemical vapour deposition) using H_2 and NH_3 as the carrier gas of the precursors and the nitridation source, respectively. Although the Mg activation process is not yet fully understood, it is widely believed that H impurities incorporated in the growth or annealing process passivate Mg acceptors by forming Mg–H neutral complexes [67]. Observation of a LVM for a Mg–N–H complex by means of IR absorption in as-grown Mg-doped films supports this hypothesis [68].

Harima *et al* [69, 70] observed Raman spectra of Mg-doped GaN MOCVD films with post-annealing in a N_2 atmosphere in the range 500–1000 °C as shown in figure 7. Here, the spectra are normalized by the peak height of the E_2^H mode at 568 cm^{-1} (scaled out to focus on weaker modes), and (a)–(c) show different frequency regions. In all panels, the bottom spectra derive from a pre-anneal film, which is highly resistive. When the sample is annealed, various new features appear, as seen in the upper traces: LVMs appear at 657 and 260 cm^{-1} upon annealing at above 600 °C, together with a broad band in the low-frequency region below $\sim$400 cm^{-1}. These features are most clearly observed for annealing at 800–900 °C, but become weak again for annealing at 1000 °C. The broad band below 400 cm^{-1} is not a phonon signal, but an electronic signal attributed to what is called the 'inter-valence-band transition of the hole', as described later. That is, the appearance of this broad band is evidence of p-type conductivity [71–73]. The 657 cm^{-1} peak is assigned to the LVM for the Mg (activated)–N bond, because

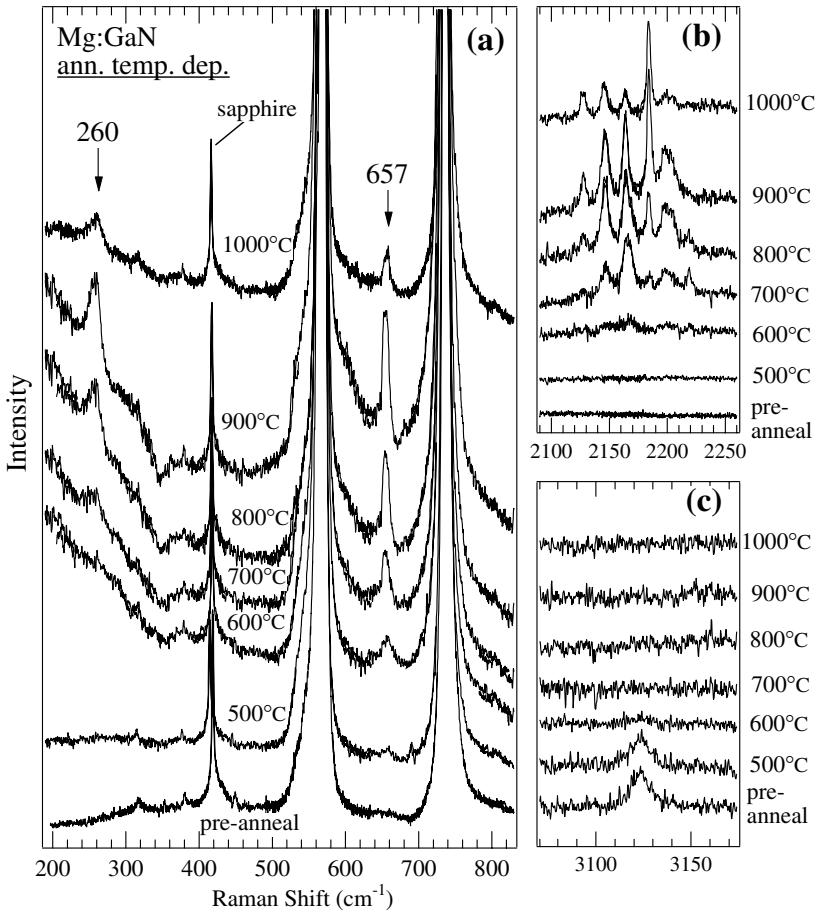

Figure 7. Raman spectra of Mg-doped wurtzite GaN films prepared by MOCVD with post-annealing at different temperatures in N_2 ambient [69, 70]. The spectra are separated into three regions, (a)–(c). The bottom spectrum in each figure was obtained from the as-grown (pre-anneal) sample.

(i) the frequency agrees with an estimate from the optical mode frequency of GaN ($\sim$560 cm^{-1}), obtained by considering the difference in reduced mass between the Mg–N and Ga–N pairs; and

(ii) the mode intensity is almost proportional to the hole density.

It is found that Mg-doped GaN films grown by MBE (molecular beam epitaxy) have native p-type character [74]. It is not surprising, then, that the 657 cm^{-1} mode is observed even in as-grown MBE films. The other peak at 260 cm^{-1} that appeared upon annealing probably has the same origin. Thus, figure 7(a) shows that p-type conductivity is obtained by annealing at 600–900 °C, but weakened by annealing at 1000 °C or above.

The high-frequency-range spectra in figures 7(b) and (c) suggest a role of H impurities in the Mg activation process [70]. A LVM is observed at 3123 cm^{-1} in (c) in a pre-anneal sample. The mode disappears upon annealing at above $\sim$600 °C, while many new LVMs appear simultaneously at 2000–2200 cm^{-1} as seen in (b). The 3123 cm^{-1} mode was verified to be H related by a deuteration experiment [68]. This frequency, being close to that of N–H

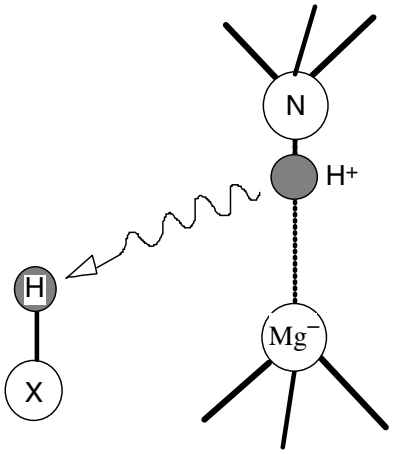

Figure 8. A schematic diagram of the Mg activation process in GaN caused by thermal annealing in a N_2 atmosphere.

stretching in NH_3, suggests that H atoms are bonded to N to form a Mg–N–H complex. This picture was supported by theoretical studies showing that H ions will be bonded to N and located at the anti-bonding site [75, 76] or body-centre site [77] of the Mg–N bonds. The LVMs at 2000–2200 cm^{-1} were observed also in as-grown MBE films that showed p-type conductivity [74, 78, 79]. These modes were attributed to H-decorated N vacancies (V_N) or extended defects. Ga–H and Mg (neutral)–H pairs [80] or more complicated centres [81] are also candidates for giving rise to these LVMs. To summarize, figure 7 shows that H atoms connected to Mg–N bonds in as-grown films are released by annealing at above 600 °C, activating the Mg acceptors. Hydrogen atoms then diffuse in the host lattice until they find new bonding partners, or get out of the film. Figure 8 shows our picture. If N_2 gas is used instead of H_2 as the carrier gas in the MOCVD growth process, the 657 cm^{-1} mode appears even in as-grown film, while hydrogen-related modes are absent [70]. This is consistent with its native p-type conductivity [82]. Other LVMs in GaN related to Ga vacancies [83–85], and impurities of arsenic [86, 87], oxygen [88], and CH_n complexes [89, 90] have been reported.

Let us move on to considering structural defects observed by means of Raman scattering. Figure 9 shows typical spectral variation in GaN induced by ion implantation and subsequent annealing [91]: here, the top trace shows a standard spectrum of hexagonal n-type GaN, giving a sharp E_2^H phonon peak at ∼570 cm^{-1} and an A_1(LO) peak at ∼750 cm^{-1}. Note that the latter peak is broadened due to a coupling with plasmon as explained later. When the sample is implanted with Ca^+, the spectrum changes drastically, as seen at the bottom, where: broad bands appear at below 350 cm^{-1} and at 500–800^{-1}; new weak signals appear at 300, 360, 420, and 670 cm^{-1}; and the E_2^H and the A_1(LO) modes are severely broadened with tails to the lower-frequency side. All these spectral features were well reproduced on implanting other species such as Ar^+. Thus, the signals are interpreted as defect-induced modes. The peaks at 360 and 420 cm^{-1} were assigned to LVMs due to N or Ga vacancies. In contrast, the peaks at 300 and 670 cm^{-1} as well as the broad signals at ∼560 and 730 cm^{-1} near the E_2^H and the A_1(LO) modes should be assigned to DARS, because they reflect characteristic features in the phonon density of states [14, 92]. The middle four traces in figure 9 were obtained by subsequent annealing at 900–1150 °C. The defect-induced modes are weakened with the rise

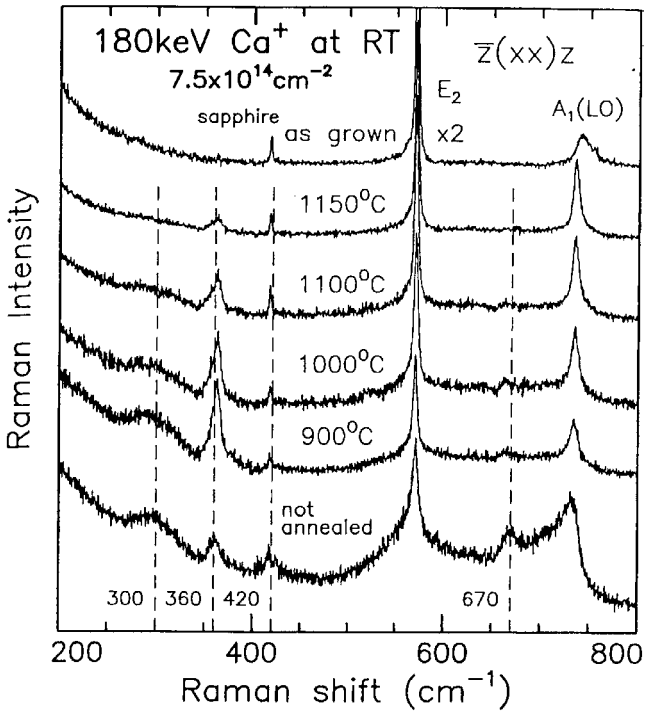

Figure 9. Raman spectra of wurtzite GaN with Ca^+ implantation and subsequent annealing [91].

of temperature, which means recovery in crystallinity. It is worth mentioning, however, that the peak for the A_1(LO) mode is still sharp even after 1150 °C annealing, and the original broad peak in the top trace is not yet recovered. This is because the coupling with the plasmon is suppressed, which suggests that the carrier mobility is low or, in other words, recovery of the crystallinity is still incomplete.

2.5. Phonon-related topics—temperature effects, superlattices, dilute magnetic semiconductors

Heating or cooling of a sample causes spectral changes similar to those induced by hydrostatic pressure on crystals: heating of a crystal induces lattice dilation, then the restoring force of lattice vibration decreases and the phonon peak shifts to lower frequency; if it is cooled, the reverse will occur. Besides the frequency shift, heating induces peak broadening because anharmonic interactions between phonons will increase, or, in other words, the phonon decay channel increases. Link *et al* [93] reported temperature effects on the E_2^H and the A_1(LO) modes in hexagonal AlN and GaN grown on sapphire in the range 85–760 K. They analysed the frequency shift considering the lattice dilation effect, anharmonic coupling of phonons up to the fourth order, and thermal strain between the nitride layer and the substrate, and showed the first two gave dominant contributions at high temperatures. The broadening was also analysed by considering up to the fourth order of anharmonic interactions. Similar results were reported for the E_2^H mode of hexagonal GaN grown on sapphire or 6H-SiC substrate [94, 95]. Link *et al* [93] observed heating of a GaN-based LED during operation by using the frequency shift of the E_2^H mode of GaN for temperature calibration.

Raman spectra of semiconductor superlattices (SLs) were intensively studied for GaAs-based systems such as GaAs/AlAs: when compared with bulk crystals, SLs present various characteristic features—zone folding of the phonon dispersion, mode confinement of optical phonons, the advent of interface modes, and so on [96]. In contrast to the case for GaAs-based materials, Raman scattering experiments on GaN-based SLs are very scarce. This is mainly due to the difficulty of the growth process and the analysis: the nitride SL is a heavily strained system, and lack of a smooth hetero-epitaxial interface and a large piezoelectric field at the interface complicate the interpretation of experimental results. So far, Chen *et al* [97] have observed zone folding of optical phonon modes in GaN/AlGaN SLs, and Gleize *et al* [98] reported quasi-confined and interface modes in a GaN/AlN SL. More recently, Davydov *et al* examined several GaN/AlGaN SLs, and reported that only the A_1(TO) mode is propagating, while other optical modes are confined. Folded acoustic phonon modes were also clearly observed [99]. Strain effects have been investigated in SLs of GaN/AlN [100] and GaN/AlGaN [99].

Dilute magnetic semiconductors (DMSs) based on III–V compounds, such as $In_{1-x}Mn_xAs$ and $Ga_{1-x}Mn_xAs$, have recently garnered much interest as candidate materials for future spin electronics or 'spintronics' applications [101]. The basic idea of spintronics is to open a new field for semiconductor devices by hybridization of spins of doped magnetic impurities with electric charges of free carriers. Although the observed ferromagnetic transition temperature has been relatively low ($T_c < 110$ K) in the above compounds, recent theoretical studies [102, 103] on wide-bandgap semiconductors were very encouraging because they predicted T_c well above 300 K, and promising experimental data began to appear on GaN-based systems [104, 105]. At present, however, Raman scattering experiments on nitride-based DMSs are still very few. Zajcac *et al* reported Raman spectra of $Ga_{1-x}Mn_xN$ with $x = 0.005$. They showed features of DARS, suggesting the difficulty of growing high-quality crystals with doping with magnetic elements [106].

3. Electronic properties

3.1. LO phonon–plasmon coupled modes

Semiconductors contain a variety of electronic excitations due to free and bound charges, and many of them can be studied by means of Raman scattering (so-called electronic Raman scattering) [107, 108]. We can observe electronic excitations due to free carriers, either single-particle excitation or collective excitation (plasmons), as well as coupled modes of electronic excitation and lattice vibration: a good example of a coupled mode is the so-called LO phonon–plasmon coupled mode (LOPC), which has been intensively studied in n-type GaN as described below [20, 109].

The LOPC mode consists of upper- and lower-frequency branches (denoted here as L^+ and L^-, respectively). Figure 10 shows typical variations of LOPC-mode profiles in n-type hexagonal GaN with the carrier density [110]. Here, the carrier density n and the mobility μ evaluated from Hall measurements are given in each figure. On increasing n from 1.2×10^{17} cm^{-3} (top) to 6.2×10^{18} cm^{-3} (bottom), the L^+ mode shifts to higher frequency and broadens, with a tail to higher frequency. The L^- mode also shifts to higher frequency. However, although this is not clear in figure 10, the L^--mode profile sharpens unlike the L^+-mode one at larger n (10^{19}–10^{20} cm^{-3}) and approaches the A_1(TO) phonon frequency at 531 cm^{-1} [109]. The solid and dashed lines are theoretical fits to the observed profile to be explained later. Variations of the L^+-and L^--mode frequencies are plotted against n in figure 11 [20, 109, 110].

The dotted line shows the plasmon frequency ω_p given by

$$\omega_p = \{4\pi ne^2/(\varepsilon_\infty m^*)\}^{1/2} \tag{5}$$

where ε_∞ (=5.35) is the optical dielectric constant of GaN, and m^* (=$0.2m_0$) is the effective mass of the electron [111]. The solid curves in figure 11 denote longitudinal excitation frequencies calculated by equating the dielectric function $\varepsilon(\omega)$ to

$$\varepsilon(\omega) = \varepsilon_\infty\{1 + (\omega_L^2 - \omega_T^2)/(\omega_T^2 - \omega^2 - \mathrm{i}\omega\Gamma) - \omega_p^2/(\omega^2 - \mathrm{i}\omega\gamma)\} = 0. \tag{6}$$

Here, ω_T (ω_L) is the TO (LO) phonon frequency in the uncoupled sample, and Γ (γ) is the damping rate of the phonon (plasmon). If Γ and γ are neglected in the present calculation, then equation (6) is solved as

$$\omega_\pm^2 = \{\omega_L^2 + \omega_p^2\}/2 \pm \{[\omega_p^2 - \omega_L^2]^2 + 4\omega_p^2[\omega_L^2 - \omega_p^2]\}^{1/2}/2. \tag{7}$$

Equation (7) reproduces the observed LOPC-mode frequencies fairly well as seen in figure 11, the sign $\pm$ corresponding to the L^+ and L^- modes, respectively.

Figure 11 suggests that the carrier density n can be estimated from the observed LOPC-mode peak frequency for either the L^+ or the L^- branch. A convenient empirical formula has been proposed for deducing n ($\lesssim 1 \times 10^{19}$ cm^{-3}) from the observed frequency shift $\Delta\omega$ (cm^{-1}) of the L^+-mode frequency from the uncoupled-mode one [112]:

$$n = 1.1 \times 10^{17}\,\Delta\omega^{0.764}. \tag{8}$$

For a more precise evaluation of the carrier density n as well as the drift mobility μ, a line-shape fitting analysis based on a semi-classical approach considering the contribution of deformation potential (DP) and electro-optical (EO) mechanisms can be employed: the Raman scattering efficiency is then described as [113, 114]

$$I(\omega) = SA(\omega)\,\mathrm{Im}[-1/\varepsilon(\omega)] \tag{9}$$

where ω is the Raman shift, S is a proportionality constant, $\varepsilon(\omega)$ is the dielectric function, and $A(\omega)$ is given by

$$\begin{aligned} A(\omega) = 1 + 2C\omega_T^2[\omega_P^2\gamma(\omega_T^2 - \omega^2) - \omega^2\Gamma(\omega^2 + \gamma^2 - \omega_P^2)]/\Delta \\ + C^2(\omega_T^4/\Delta)[\omega_P^2\{\gamma(\omega_L^2 - \omega_T^2) + \Gamma(\omega_P^2 - 2\omega^2)\} + \omega^2\Gamma(\omega^2 + \gamma^2)]/(\omega_L^2 - \omega_T^2). \end{aligned} \tag{10}$$

Here, C is the Faust–Henry coefficient [115] for hexagonal GaN [20, 110, 116]. We can fit the observed line shape with equation (9) using n, Γ, and γ as adjustable parameters, and deduce the carrier density n as well as the mobility μ from the relation $\mu = e/(m^*\gamma)$. In figure 10, the smooth solid curves show the best-fit calculations obtained by assuming $\omega_T = 533$ cm^{-1}, $\omega_L = 735$ cm^{-1}, $C = 0.48$ [110], and (n (cm^{-3}), μ (cm^2 V^{-1} s^{-1})) = (0.9×10^{17}, 467), (2.7×10^{17}, 333), (0.8×10^{18}, 211), and (3.6×10^{18}, 123) for samples (a)–(d), respectively. There is a good agreement as regards the spectral profile as well as the carrier density and mobility between the simulation and the observation. Although there is still a noticeable discrepancy for the L^- branch of (d), having the largest carrier density, we can improve the agreement by including a charge-density-fluctuation (CDF) mechanism [113, 114] into the calculation as shown by the dashed curve [110, 117]. Similar results were previously reported for n-type GaAs [118], in which the CDF mechanism gave comparable contributions to the DP and EO mechanisms. It has been suggested that the CDF contribution is generally important when carriers have small effective mass and small damping [107].

Figure 12, upper figure, shows Raman spectra observed from backscattering from the c-plane of Mg-doped p-type GaN samples [73]. The upper four samples were post-annealed in a N_2 atmosphere at 800 °C and have different hole densities. In contrast, the bottom one

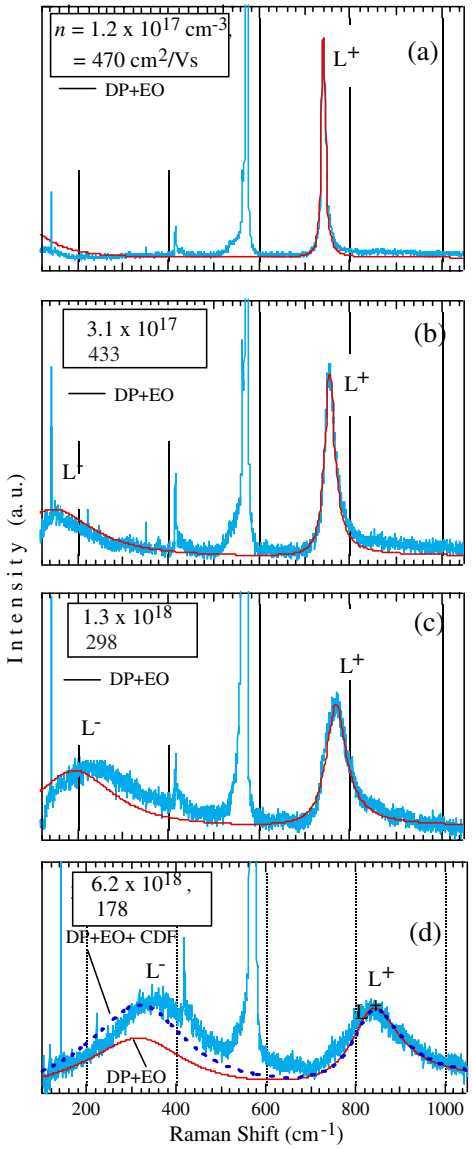

Figure 10. Raman spectra of n-type wurtzite GaN with different carrier densities [110]. Smooth solid lines denote theoretical fits for the L^+ mode, considering DP and EO mechanisms. The dashed line in (d) includes the CDF contribution.

was not annealed; it is therefore highly resistive, and was shown for comparison. The carrier density p (cm^{-3}) and mobility μ ($cm^2\ V^{-1}\ s^{-1}$) obtained from Hall measurements are shown in the figure. Contrary to the case for n-type GaN, there is no LOPC-mode feature for the A_1(LO) mode; the profile is always sharp and gives no clear frequency shift or broadening with increase of p. This was attributed to heavy damping of the hole plasmon [73, 116, 119].

Other nitride semiconductors have not yet been well investigated from the viewpoint of LO phonon–plasmon coupling. N-type cubic GaN showed heavy damping of plasmons [120]. This is probably to be ascribed to its more defective nature compared to hexagonal GaN.

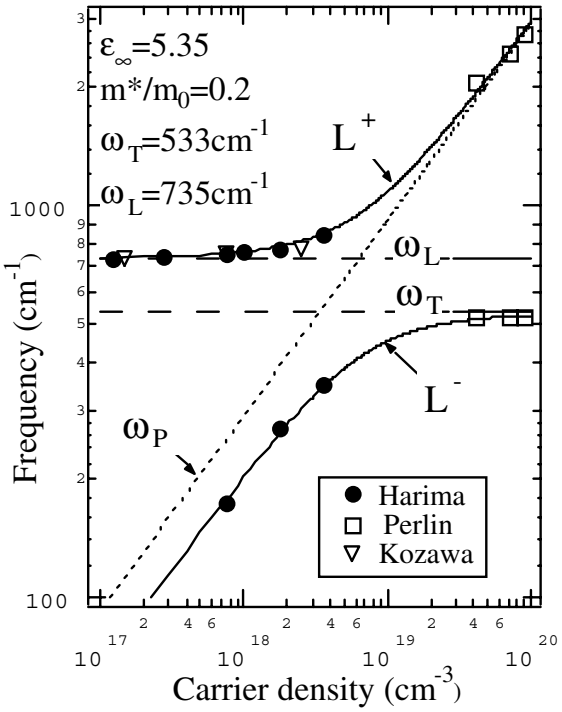

Figure 11. The carrier-density dependence of the axial LOPC-mode frequency in n-type wurtzite GaN. The data are derived from Harima *et al* (filled circles) [110], Perlin *et al* (squares) [109] and Kozawa *et al* (triangles) [20].

3.2. Inter-valence-band transitions

In figure 12, upper figure, the annealed samples show a broad band in the low-frequency region at $<\sim 400\ \mathrm{cm}^{-1}$, the intensity of which increases with the hole density. This band was assigned to a single-particle excitation of a hole from the heavy-hole band to the light-hole band (inter-valence-band transition) [73]. This type of electronic excitation was previously reported in heavily doped p-type Si and GaAs [71, 72]. The continuum band intensity normalized by the E_2^L phonon peak intensity at 144 cm^{-1}, I_B/S, is plotted in the lower figure as filled circles. The systematic variation of the band intensity (dashed line) can be used for calibrating the hole density. Since the LOPC-mode analysis is not possible for p-type GaN, this calibration technique is of practical importance.

4. Other topics

4.1. Resonant Raman scattering—quantum wells, quantum dots

Resonant enhancement of the Raman scattering in semiconductors occurs when the incident or scattered photon energy coincides with the bandgap of the specimen, or, in other words, when there is efficient electronic excitation in the specimen [11]. Resonant enhancement enables observation of the Raman signal from a limited scattering volume, which is too weak to be observed under off-resonant conditions. For this reason, resonant Raman scattering has recently increased in importance as a tool for characterizing nanometre-scale structures such as QWs and quantum dots (QDs).

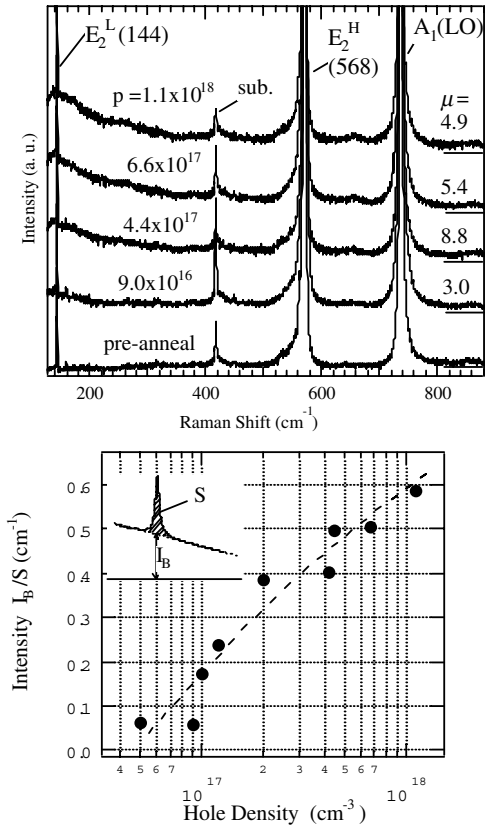

Figure 12. Raman spectra of Mg-doped p-type hexagonal GaN with different hole densities (upper figure) [73]. The lower figure shows variation of the low-frequency continuum band. The dashed curve is a guide to the eye.

Wagner and co-workers reported a series of resonant Raman studies on various layered structures of the hexagonal GaN-based system [50, 121–124]. The merit of resonant Raman scattering is seen typically in figure 13: here, Raman spectra from a QW structure of $Al_{0.15}Ga_{0.85}N$ (100 nm)/GaN (3 nm)/$Al_{0.15}Ga_{0.85}N$ (1500 nm) in the on-resonant (top trace) and off-resonant (middle) conditions are compared [122]. The bottom trace is a standard GaN bulk signal given for comparison. In the off-resonant case, the LO phonon region is dominated by the signal of the AlGaN barrier layers at 770 cm^{-1}. In the resonant case, in contrast, the incident laser at 3.54 eV induces resonance enhancement in the GaN well layer; thus the well layer signal at 740 cm^{-1} is greatly enhanced. Considering that the well layer is much thinner than the barrier layers, the resonant enhancement effect is remarkable. In InGaN alloys, compositional fluctuation [123] and a strain-induced piezoelectric field in InGaN/GaN QWs [124] have been investigated by means of visible lasers. Resonant Raman scattering in GaN QDs has also recently been reported [125, 126], and quantum size effects discussed [125].

4.2. Micro-Raman imaging

Micro-Raman imaging, i.e., mapping of the Raman microprobe signal or its derivatives, has become a standard Raman characterization technique for getting a quick overview of spatial

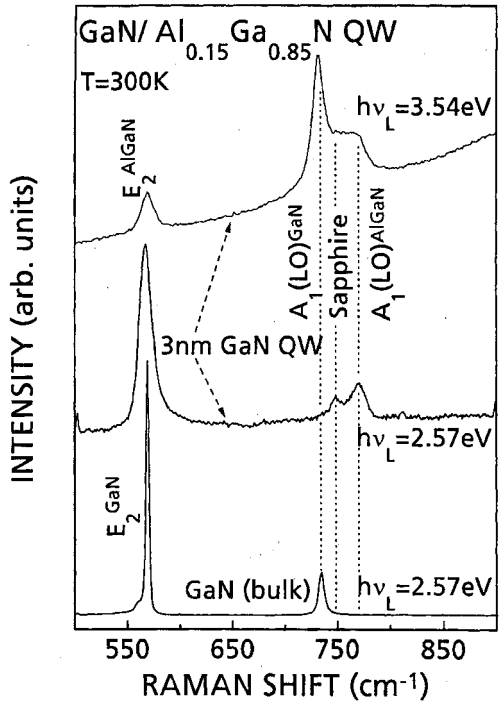

Figure 13. Raman spectra of wurtzite $Al_{0.15}Ga_{0.85}N/GaN/Al_{0.15}Ga_{0.85}N$, a single QW (middle and top), and GaN for reference (bottom) [122].

variation of various physical quantities in a specimen [127]. This technique has been applied to nitride semiconductors for characterizing the distribution of strain, carrier concentration, polytype (cubic or hexagonal), crystalline defect, and so on. Since only an outline is given here, readers are strongly recommended to see the original articles with beautiful (often colourful) mappings.

LOPC modes and the E_2^H phonon modes in hexagonal GaN have been most frequently examined for the mapping of carrier density and lattice strain, respectively. Ponce *et al* observed LOPC modes with a spatial resolution of 0.5 μm in an n-type GaN layer, and analysed the donor impurity distribution [128]. Harima *et al* analysed LOPC modes in an n-type GaN layer, and found that the distributions of carrier density and mobility were strongly correlated with the direction of source-gas flow [129]. Siegle *et al* observed the cross-section of an undoped 220 μm thick GaN layer grown by hydride vapour phase epitaxy (HVPE) on sapphire and compared between Raman scattering and microscopic PL data [130]: their Raman study showed variation of the carrier density from 10^{17} cm^{-3} (near surface) to 10^{20} cm^{-3} (interface with substrate) and relaxation of the biaxial compressive strain toward the surface. The PL peak showed a gradual red-shift toward the interface and a sudden blue-shift at the interface. These effects were explained by a stress gradient and an inhomogeneous carrier distribution. Goldys *et al* also reported high carrier density near the interface in a thick HVPE film [131]. Siegle *et al* compared signal intensities between the E_2^H- and the A_1(TO) phonon modes by observing the cross-section of a 400 μm thick HVPE film, and showed reorientation of the *c*-axis near the interface [132]. Mixing of cubic and hexagonal GaN phases in an epitaxial layer was also studied by comparing characteristic phonon signals [133].

Raman imaging study of GaN layers grown by the epitaxial lateral overgrowth (ELOG) technique is a rapidly increasing area. Improved spatial resolution achieved with the confocal microscopy technique [127] revealed unintentional doping of Si impurities that derive from the mask of SiN [134] and SiO_x [135]. Holtz *et al* observed isolated hexagonal islands grown on a square-patterned mask, and found large biaxial compressive strain and small carrier density in the window region [136]. Bertram *et al* characterized ELOG-grown layers combining Raman scattering with cathode luminescence imaging, and showed that a coherent growth region having good crystallinity was dominated by narrow excitonic emission [137].

5. Concluding remarks

Owing to the rapid development in the growth technology, we have seen in the last decade dramatic developments in Raman scattering studies on nitride semiconductors. Typical results are as follows: Γ-point phonon frequencies identified for both hexagonal and cubic GaN, AlN, and InN; compositional variation of the phonon frequency in ternary alloys of AlGaN and InGaN; stress and temperature variations of the phonon frequency in GaN and AlN; impurity and defect modes observed. LOPC modes in n-type GaN have also been well studied and widely applied in evaluation of the carrier density distribution using the Raman imaging technique.

There still remain, however, many important issues for further Raman studies. First, basic phonon data on In-rich compounds are insufficient for both ternary alloys and binary compounds (InN) due to the difficulty in the growth process. Similarly, phonon data on cubic GaN, AlN, and InN are limited. For cubic ternary alloys, the situation is worse. Second, the LOPC modes have been well studied only for n-type hexagonal GaN, and those for other compounds have scarcely been examined. Such reports for n-type InGaN and AlGaN are eagerly awaited, because optical characterization of the free-carrier density and mobility in these alloys is important for the development of devices. Third, there will be increasing interest in lattice properties of low-dimensional systems such as QWs, superlattices, and QDs, because these materials are all also key elements for future devices. When compared with GaAs-based systems that have been relatively well explored, nitride systems have intrinsic complexity such as large strain and a piezoelectric field at the hetero-epitaxial interface. Fourth, electronic Raman scattering due to free and bound charges is very scarcely reported. LOPC provides an exceptional case. The p-type materials have been especially poorly studied (both binary and ternary compounds). Electronic transitions related to shallow impurity levels have not yet been clearly observed by means of Raman scattering. Optical characterization of free-electron motion in low-dimensional systems such as the two-dimensional electron gas (2DEG) at a hetero-epitaxial interface will attract much attention from the viewpoint of device applications.

Although there is a long way to go, Raman scattering will undoubtedly remain a powerful technique for exploring physics in nitride semiconductors, and a convenient characterization tool for use in developing future devices.

References

[1] Strite S and Morkoç H 1992 *J. Vac. Sci. Technol.* B **10** 1237–65
[2] Morkoç H, Strite S, Gao G B, Lin M E, Sverdlov B and Burns M 1994 *J. Appl. Phys.* **76** 1363–98
[3] Pearton S J, Zolper J C, Shul R J and Ren F 1999 *J. Appl. Phys.* **86** 1–78
[4] Davydov V Yu, Klochikhin A A, Seisyan R P, Emtsev V V, Ivanov S V, Bechstedt F, Furthmuller J, Harima H, Mudryi A V, Aderhold J, Semchinova O and Graul J 2002 *Phys. Status Solidi* b **229** R1–3

[5] Wu J, Walukiewicz W, Yu K M, Ager J W III, Haller E E, Lu H, Schaff W J, Saito Y and Nanishi Y 2002 *Appl. Phys. Lett.* **80** 3967–9

[6] Sze S M 1981 *Physics of Semiconductor Devices* 2nd edn (New York: Wiley) pp 849–51

[7] Pankove J I and Moustakas T D (ed) 1998 *Gallium Nitride I (Semiconductors and Semimetals vol 50)* (San Diego, CA: Academic)

[8] Pankove J I and Moustakas T D (ed) 1999 *Gallium Nitride II (Semiconductors and Semimetals vol 57)* (San Diego, CA: Academic)

[9] Jain S C, Willander M, Narayan J and Van Overstraeten R 2000 *J. Appl. Phys.* **87** 965–1006

[10] Morkoç H 1999 *Nitride Semiconductors and Devices (Springer Series in Material Science vol 32)* ed R Hull, R M Jr Osgood, H Sakaki and Z Zunger (Berlin: Springer)

[11] Cardona M 1982 *Light Scattering in Solids II (Springer Topics in Applied Physics vol 50)* ed M Cardona and G Güntherodt (Berlin: Springer) pp 19–178

[12] Loudon R 1964 *Adv. Phys.* **13** 423–82

[13] Harima H, Sakashita H and Nakashima S unpublished

[14] Davydov V Yu, Kitaev Yu E, Goncharuk I N, Smirnov A N, Graul J, Semchinova O, Uffmann D, Smirnov M B, Mirgorodsky A P and Evarestov R A 1998 *Phys. Rev.* B **58** 12 899–907

[15] Argüello C A, Rousseau D L and Porto S P S 1969 *Phys. Rev.* **181** 1351–63

[16] Manchon D D, Barker A S, Dean P J and Zetterstrom R B 1970 *Solid State Commun.* **8** 1227–31

[17] Burns G, Dacol F, Marinace J C, Scott B A and Burstein E 1973 *Appl. Phys. Lett.* **22** 356–8

[18] Cingolani A, Ferrara M, Lugara M and Scamarcio G 1986 *Solid State Commun.* **58** 823–4

[19] Perlin P, Carillon C J, Itie J P, Miguel A S, Grzegory I and Polian A 1992 *Phys. Rev.* B **45** 83–9

[20] Kozawa T, Kachi T, Kano H, Taga Y and Hashimoto M 1994 *J. Appl. Phys.* **75** 1098–101

[21] Azuhata T, Sota T, Suzuki K and Nakamura S 1995 *J. Phys.: Condens. Matter* **7** L129–33

[22] Tabata A, Enderlein R, Leite J R, da Silva S W, Galzerani J C, Schikora D, Kloidt M and Lischka K 1996 *J. Appl. Phys.* **79** 4137–40

[23] Brafman O, Lengyel G, Mitra S S, Gielisse J N, Plendl J N and Mansur L C 1968 *Solid State Commun.* **6** 523–6

[24] Sanjuro J A, Cruz E L, Vogl P and Cardona M 1983 *Phys. Rev.* B **28** 4579–84

[25] Carlone C, Lakin K M and Shanks H R 1984 *J. Appl. Phys.* **55** 4010–14

[26] Hayashi K, Itoh K, Sawaki N and Akasaki I 1991 *Solid State Commun.* **77** 115–18

[27] McNeil L E, Grimsditch M and French R H 1993 *J. Am. Ceram. Soc.* **76** 1132–5

[28] Perlin P, Polian A and Suski T 1993 *Phys. Rev.* B **47** 2874–7

[29] Siegle H, Eckey L, Hoffmann A, Thomsen C, Meyer B K, Schikora D, Hankeln M and Lischka K 1995 *Solid State Commun.* **96** 943–9

[30] Harima H, Inoue T, Nakashima S, Okumura H, Ishida Y, Yoshida S, Koizumi T, Grille H and Bechstedt F 1999 *Appl. Phys. Lett.* **74** 191–3

[31] Davydov V Yu, Emtsev V V, Goncharuk I N, Smirnov A N, Petrikov V D, Mamutin V V, Vekshin V A, Ivanov S V, Smirnov M B and Inushima T 1999 *Appl. Phys. Lett.* **75** 3297–9

[32] Kaczmarczyk G, Kaschner A, Reich S, Hoffmann A, Thomsen C, As D J, Lima A P, Schikora D, Lischka K, Averbeck R and Riechert H 2000 *Appl. Phys. Lett.* **76** 2122–4

[33] Tabata A, Lima A P, Teles L K, Scolfaro L M R, Leite J R, Lemos V, Schöttker B, Frey T, Schikora D and Lischka K 1999 *Appl. Phys. Lett.* **74** 362–4

[34] Davydov V Yu, Averkiev N S, Goncharuk I N, Nelson D K, Nikitina I P, Polkovnikov A S, Smirnov A N, Jacobson M A and Semchinova O K 1997 *J. Appl. Phys.* **82** 5097–102

[35] Bergman L, Dutta M, Balkas C, Davis R F, Christman J A, Alexson D and Nemanich R J 1999 *J. Appl. Phys.* **85** 3535–9

[36] Azuhata T, Ono M, Torii K, Sota T, Chichibu S and Nakamura S 2000 *J. Appl. Phys.* **88** 5202–5

[37] Siegle H, Kaczmarczyk G, Filippidis L, Litvinchuk A P, Hoffmann A and Thomsen C 1997 *Phys. Rev.* B **55** 7000–4

[38] Murugkar S, Merlin R, Botchkarev A, Salvador A and Morkoç H 1995 *J. Appl. Phys.* **77** 6042–3

[39] Azuhata T, Matsunaga T, Shimada K, Yoshida K, Sota T, Suzuki K and Nakamura S 1996 *Physica* B **219/220** 493–5

[40] Karch K, Wagner J-M and Bechstedt F 1998 *Phys. Rev.* B **57** 7043–9

[41] Nakamura S 1998 *Gallium Nitride I (Semiconductors and Semimetals vol 50)* ed J I Pankove and T D Moustakas (San Diego, CA: Academic) pp 431–57

[42] Grille H and Bechstedt F 1996 *J. Raman Spectrosc.* **27** 201–5

[43] Grille H, Schnittler Ch and Bechstedt F 2000 *Phys. Rev.* B **61** 6091–105

[44] Cros A, Angerer H, Handschuh R, Ambacher O, Stutzmann M, Höpler R and Metzger T 1997 *Solid State Commun.* **104** 35–9

[45] Demangeot F, Groenen J, Frandon J, Renucci M A, Briot O, Clur S and Aulombard R L 1998 *Appl. Phys. Lett.* **72** 2674–6
[46] Wisniewski P, Knap W, Malzac J P, Camassel J, Bremser M D, Davis R F and Suski T 1998 *Appl. Phys. Lett.* **73** 1760–2
[47] Davydov V Yu, Goncharuk I N, Smirnov A N, Nikolaev A E, Lundin W L, Usikov A S, Klochikhin A A, Aderhold J, Graul J, Semchinova O and Harima H 2002 *Phys. Rev.* B **65** 125203
[48] Wu J, Walukiewicz W, Yu K M, Ager J W III, Haller E E, Hai Lu and Schaff W J 2002 *Appl. Phys. Lett.* **80** 4741–3
[49] Davydov V Yu, Klochikhin A A, Seisyan R P, Emtsev V V, Ivanov S V, Bechstedt F, Furthmuller J, Harima H, Mudryi A V, Aderhold J, Semchinova O and Graul J 2002 *Phys. Status Solidi* b **229** R1–3
[50] Behr D, Niebuhr R, Obloh H, Wagner J, Bachem K H and Kaufmann U 1997 *Mater. Res. Soc. Symp. Proc.* **468** 213–18
[51] Harima H, Kurimoto E, Sone Y, Nakashima S, Chu S, Ishida A and Fujiyasu H 1999 *Phys. Status Solidi* a **216** 785–8
[52] Tabata A, Leite J R, Lima A P, Silveira E, Lemos V, Frey T, As D J, Schikora D and Lischka K 1999 *Appl. Phys. Lett.* **75** 1095–7
[53] Suzuki M and Uenoyama T 1996 *J. Appl. Phys.* **80** 6868–74
[54] Christensen N E and Perlin P 1998 *Gallium Nitride I (Semiconductors and Semimetals vol 50)* ed J I Pankove and T D Moustakas (London: Academic) pp 409–29
[55] Gil B 1999 *Gallium Nitride II (Semiconductors and Semimetals vol 57)* ed J I Pankove and T D Moustakas (London: Academic) pp 209–74
[56] Kisielowski C 1999 *Gallium Nitride II (Semiconductors and Semimetals vol 57)* ed J I Pankove and T D Moustakas (London: Academic) pp 275–317
[57] Kuball K, Hayes J M, Prins A D, van Uden N W A, Dunstan D J, Ying Shi and Edgar J H 2001 *Appl. Phys. Lett.* **78** 724–6
[58] Gorczyca I and Christensen N E 1991 *Solid State Commun.* **79** 1033–4
[59] Landolt–Börnstein New Series 1982 Group III, vol 17a (Berlin: Springer)
[60] Taylor A and Jones R M 1960 Silicon carbide—a high temperature semiconductor *Proc. Conf. on Silicon Carbide (Boston, MA 1959)* ed J R O'Connor and J Smiltens (Oxford: Pergamon) pp 147–54
[61] Kisielowski C, Krüger J, Ruvimov S, Suski T, Ager J W III, Jones E, Weber Z L, Rubin M, Weber E R, Bremser M D and Davis R F 1996 *Phys. Rev.* B **54** 17 745–53
[62] Kozawa T, Kachi T, Kano H, Nagase H, Koide N and Manabe K 1995 *J. Appl. Phys.* **77** 4389–92
[63] Demangeot F, Frandon J, Renucci M A, Briot O, Gil B and Aulombard R L 1996 *Solid State Commun.* **100** 207–10
[64] Wagner J-M and Bechstedt F 2000 *Appl. Phys. Lett.* **77** 346–8
[65] Stavola M 1999 *Identification of Defects in Semiconductors (Semiconductors and Semimetals vol 51B)* ed M Stavola (London: Academic) pp 153–224
[66] Amano H, Kito M, Hiramatsu K and Akasaki I 1989 *Japan. J. Appl. Phys.* **28** L2112–14
[67] Nakamura S, Iwasa N, Senoh M and Mukai T 1992 *Japan. J. Appl. Phys.* **31** 1258–66
[68] Götz W, Johnson N, Bour D, McCluskey M and Haller E 1996 *Appl. Phys. Lett.* **69** 3725–7
[69] Harima H, Inoue T, Nakashima S, Ishida M and Taneya M 1999 *Appl. Phys. Lett.* **75** 1383–5
[70] Harima H, Inoue T, Sone Y, Nakashima S, Ishida M and Taneya M 1999 *Phys. Status Solidi* b **216** 789–93
[71] Cerdeira F, Fjeldly T A and Cardona M 1973 *Phys. Rev.* B **8** 4734–45
[72] Olego D and Cardona M 1981 *Phys. Rev.* B **23** 6592–602
[73] Harima H, Inoue T, Nakashima S, Furukawa K and Taneya M 1998 *Appl. Phys. Lett.* **73** 2000–2
[74] Kaschner A, Siegle H, Kaczmarczyk G, Strassburg M, Hoffmann A, Thomsen C, Birkle U, Einfeldt S and Hommel D 1999 *Appl. Phys. Lett.* **74** 3281–3
[75] Neugebauer J and Van de Walle C G 1995 *Phys. Rev. Lett.* **75** 4452–5
[76] Torres V J B, Cerg S and Jones R 1997 *MRS Internet J. Nitride Semicond. Res.* **2** 35
[77] Okamoto Y, Saito M and Oshiyama A 1996 *Japan. J. Appl. Phys.* **35** L807–9
[78] Brandt M S, Ager J W III, Götz W, Johnson N M, Harris J S Jr, Molnar R J and Moustakas T D 1994 *Phys. Rev.* B **49** 14 758–61
[79] Kaschner A, Kaczmarczyk G, Hoffmann A, Thomsen C, Birkle U, Einfeldt S and Hommel D 1999 *Phys. Status Solidi* b **216** 551–5
[80] Pearton S J, Corbett J W and Stavola M 1992 *Hydrogen in Crystalline Semiconductors (Springer Series in Materials Science vol 23)* ed U Gonser, A Mooradian, R M Osgood, M B Panish and H Sakaki (Berlin: Springer) pp 102–345
[81] Reboredo F A and Pantelides S T 1999 *Phys. Rev. Lett.* **82** 1887–90

[82] Sugiura L, Suzuki M and Nishino J 1998 *Appl. Phys. Lett* **72** 1748–50
[83] Duan Q, Zhang B R, Zhang Y X, Wang L P, Qin G G, Zhang G Y, Tong Y Z, Jin S X, Yang Z J, Zhang X and Xu Z H 1997 *J. Appl. Phys.* **82** 5745–7
[84] Weinstein M G, Song C Y, Stavola M, Pearton S J, Wilson R G, Shul R J, Killeen K P and Ludowise M J 1998 *Appl. Phys. Lett.* **72** 1703–5
[85] Van de Walle C G 1997 *Phys. Rev.* B **56** 10 020–3
[86] Siegle H, Kaschner A, Hoffmann A, Broser I and Thomsen C 1998 *Phys. Rev.* B **58** 13 619–26
[87] Kaczmarczyk G, Kaschner A, Hoffmann A and Thomsen C 2000 *Phys. Rev.* B **61** 5353–7
[88] Wetzel C, Amano H, Akasaki I, Ager J W III, Grzegory I, Topf M and Meyer B K 2000 *Phys. Rev.* B **61** 8202–6
[89] Yi G-C and Wessels B W 1997 *Appl. Phys. Lett.* **70** 357–9
[90] Manasreh M O, Baranowski J M, Pakula K, Jiang H X and Lin J 1999 *Appl. Phys. Lett.* **72** 659–61
[91] Limmer W, Ritter W, Sauer R, Mensching B, Liu C and Rauschenbach B 1998 *Appl. Phys. Lett.* **72** 2589–92
[92] Nipko J C, Loong C-K, Balkas C M and Davis R F 1998 *Appl. Phys. Lett.* **73** 34–6
[93] Link A, Bitzer K, Limmer W, Sauer R, Kirchner C, Schwegler V, Kamp M, Ebling D G and Benz K W 1999 *J. Appl. Phys.* **86** 6256–60
[94] Li W S, Shen Z X, Feng Z C and Chua S J 2000 *J. Appl. Phys.* **87** 3332–7
[95] Giehler M, Ramsteiner M, Waltereit P, Brandt O, Ploog K H and Obloh H 2001 *J. Appl. Phys.* **89** 3634–41
[96] Jusserand B and Cardona M 1989 *Light Scattering in Solids V (Springer Topics in Applied Physics vol 66)* ed M Cardona and G Güntherodt (Heidelberg: Springer) pp 49–152
[97] Chen C H, Chen Y F, Shih An, Lee S C and Jiang H X 2001 *Appl. Phys. Lett.* **78** 3035–7
[98] Gleize J, Frandon J, Demangeot F, Renucci M A, Kuball M, Hayes J M, Widmann F and Daudin B 2001 *Mater. Sci. Eng.* B **82** 27–9
[99] Davydov V Yu, Klochikhin A A, Goncharuk I N, Smirnov A N, Kyutt R N, Scheglov M P, Sakharov A V, Lundin W V, Zavarin E E and Usikov A S 2002 *Phys. Status Solidi* a **188** 863–6
[100] Gleize J, Demangeot F, Frandon J, Renucci M A, Widmann F and Daudin B 1999 *Appl. Phys. Lett.* **74** 703–5
[101] Ohno H 1998 *Science* **281** 951–6
[102] Dietl T, Ohno H, Matsukura F, Cibert J and Ferrand D 2000 *Science* **287** 1019–22
[103] Sato K and Katayama-Yoshida H 2001 *Japan. J. Appl. Phys.* **40** L485–7
[104] Reed M L, El-Masry N A, Stadelmaier H H, Ritums M K, Reed M J, Parker C A, Roberts J C and Bedair S M 2001 *Appl. Phys. Lett.* **79** 3473–5
[105] Thaler G T, Overberg M E, Gila B, Frazier R, Abernathy C R, Pearton S J, Lee J S, Lee S Y, Park Y D, Khim Z G, Kim J and Ren F 2002 *Appl. Phys. Lett.* **80** 3964–6
[106] Zajcac M, Doradzinski R, Gosk J, Szczytko J, Lefeld-Sosnowska M, Kaminska M, Twardowski A, Palczewska M, Grzanka E and Bicki W G 2001 *Appl. Phys. Lett.* **78** 1276–8
[107] Klein M V 1975 *Light Scattering in Solids I (Springer Topics in Applied Physics vol 1)* I ed M Cardona (Berlin: Springer) pp 147–204
[108] Abstreiter G, Cardona M and Pinczuk A 1983 *Light Scattering in Solids (Springer Topics in Applied Physics vol 54)* IV ed M Cardona and G Güntherodt (Heidelberg: Springer) pp 5–150
[109] Perlin P, Camassel J, Knap W, Taliercio T, Chervin J C, Suski T, Grzegory I and Porowski S 1995 *Appl. Phys. Lett.* **67** 2524–6
[110] Harima H, Sakashita H and Nakashima S 1998 *Mater. Sci. Forum* **264–8** 1363–6
[111] Barker A S Jr and Ilegems M 1973 *Phys. Rev.* B **7** 743–50
[112] Wetzel C, Walukiewicz W, Haller E E, Ager J III, Grzegory I, Porowski S and Suski T 1996 *Phys. Rev.* B **53** 1322–6
[113] Klein M V, Ganguly B N and Colwell P J 1972 *Phys. Rev.* B **6** 2380–8
[114] Irmer G, Toporov V V, Bairamov B H and Monecke J 1983 *Phys. Status Solidi* b **119** 595–603
[115] Faust W L and Henry C H 1966 *Phys. Rev. Lett.* **17** 1265–8
[116] Demangeot F, Frandon J, Renucci M A, Grandjean N, Beaumont B B, Massies J and Gibart P 1998 *Solid State Commun.* **106** 491–4
[117] Demangeot F, Frandon J, Renucci M A, Meny C, Briot O and Aulombard R L 1997 *J. Appl. Phys.* **82** 1305–9
[118] Mooradian A and McWhorter A L 1969 Light scattering spectra of solids *Proc. Int. Conf. on Light Scattering Spectra of Solids* ed G B Wright (Berlin: Springer) pp 297–308
[119] Popovici G, Xu G Y, Botchkarev A, Kim W, Tang H, Salvador A and Morkoç H 1997 *J. Appl. Phys.* **82** 4020–3
[120] Ramsteiner M, Brandt O and Ploog K H 1998 *Phys. Rev.* B **58** 1118–21
[121] Behr D, Wagner J, Schneider J, Amano H and Akasaki I 1996 *Appl. Phys. Lett.* **68** 2404–6
[122] Behr D, Niebuhr R, Wagner J, Bachem K-H and Kaufmann U 1997 *Appl. Phys. Lett.* **70** 363–5
[123] Behr D, Wagner J, Ramakrishnan A, Obloh H and Bachem K-H 1998 *Appl. Phys. Lett.* **73** 241–3

[124] Wagner J, Ramakrishnan A, Obloh H and Maier M 1999 *Appl. Phys. Lett.* **74** 3863–5
[125] Kuball M, Gleize J, Tanaka Satoru and Aoyagi Y 2001 *Appl. Phys. Lett.* **78** 987–9
[126] Gleize J, Demangeot F, Frandon J, Renucci M A, Kuball M, Damilano B, Grandjean N and Massies J 2001 *Appl. Phys. Lett.* **79** 686–8
[127] Barbillat J 1996 *Raman Microscopy—Developments and Applications* ed G Turrell and J Corset (London: Academic) pp 175–200
[128] Ponce F A, Steeds J W, Dyer C D and Pitt G D 1996 *Appl. Phys. Lett.* **69** 2650–2
[129] Harima H, Sakashita H, Inoue T and Nakashima S 1998 *J. Cryst. Growth* **189/190** 672–6
[130] Siegle H, Hoffmann A, Eckey L, Thomsen C, Christen J, Bertram F, Schmidt D, Rudloff D and Hiramatsu K 1997 *Appl. Phys. Lett.* **71** 2490–2
[131] Goldys E M, Paskova T, Ivanov I G, Arnaudov B and Monemar B 1998 *Appl. Phys. Lett.* **73** 3583–5
[132] Siegle H, Thurian P, Eckey L, Hoffmann A, Thomsen C, Meyer B K, Amano H, Akasaki I, Detchprohm T and Hiramatsu K 1996 *Appl. Phys. Lett.* **68** 1265–7
[133] Harima H, Inoue T, Nakashima S, Okumura H, Ishida Y, Yoshida S and Hamaguchi H 1998 *J. Cryst. Growth* **189/190** 435–8
[134] Pophristic M, Long F H, Schurman M, Ramer J and Ferguson I T 1999 *Appl. Phys. Lett.* **74** 3519–22
[135] Matthews M J, Hsu J W P, Gu S and Kuech T F 2001 *Appl. Phys. Lett.* **79** 3086–8
[136] Holtz M, Seon M, Prokofyeva T, Temkin H, Singh R, Dabkowski F P and Moustakas T D 1999 *Appl. Phys. Lett.* **75** 1757–9
[137] Bertram F, Riemann T, Christen J, Kaschner A, Hoffmann A, Thomsen C, Hiramatsu K, Shibata T and Sawaki N 1999 *Appl. Phys. Lett.* **74** 359–61